Non-diffusive nature of collisionless α-particle transport: dependence on toroidal symmetry in stellarator geometries

A. Gogoleva,[1, a)] V. Tribaldos,[1] J.M. Reynolds-Barredo,[1] R. Sánchez,[1] J. Alcusón,[2] and A. Bustos[3]

[1)]*Departamento de Física, Universidad Carlos III de Madrid, 28911 Leganés, Madrid, Spain*

[2)]*Max-Planck-Institut für Plasmaphysik, 17491 Greifswald, Germany*

[3)]*Departamento de Tecnología, CIEMAT, 28040 Madrid, Spain*

(Dated: 3 June 2020)

An adequate confinement of α-particles is fundamental for the operation of future fusion powered reactors. An even more critical situation arises for stellarator devices, whose complex magnetic geometry can substantially increase α-particle losses. A traditional approach to transport evaluation is based on a diffusive paradigm, however, a growing body of literature presents a considerable amount of examples and arguments towards the validity of non-diffusive transport models for fusion plasmas, particularly in cases of turbulent driven transport [R. Sánchez and D.E. Newman, Plasma Phys. Control. Fusion **57** 123002 (2015)]. Likewise, a recent study of collisionless α-particle transport in quasi-toroidally symmetric stellarators [A. Gogoleva *et al.*, Nucl. Fusion **60** 056009 (2020)] puts the diffusive framework into question. In search of a better transport model, we numerically characterized and quantified the underlying nature of transport of the resulting α-particle trajectories by employing a whole set of tools, imported from fractional transport theory. The study was carried out for a set of five configurations to establish the relation between the level of magnetic field toroidal symmetry and the fractional transport coefficients, i.e. the Hurst H, the spatial α and the temporal β exponents, each being a merit of non-diffusive transport. The results indicate that the α-particle ripple-enhanced transport is non-Gaussian and non-Markovian. Moreover, as the degree of quasi-toroidal symmetry increases, it becomes strongly subdiffusive. Although, the validity of the fractional model itself becomes doubtful in the limiting high and low symmetry cases.

---

a)Electronic mail: Alena.Gogoleva@uc3m.es

I. INTRODUCTION

There is still no fully satisfactory explanation of the experimental particle and energy transport across the magnetic field in fusion devices. The cost of an economically viable thermonuclear fusion powered reactor is largely determined by this radial transport that has, so far, been estimated and extrapolated using semi-empirical methods based on traditional diffusive-like models. However, it is still unclear whether these models are sufficiently complete and adequate to describe radial transport in all reactor-relevant regimes. These are pressing issues for the radial transport of α-particles, whose confinement is essential for the overall plasma performance. This transport has been assumed diffusive in the literature[1–7], which allowed to create transport models able to fit the relevant experimental data [8]. However, the diffusion paradigm rests on the assumption that transport dynamics is Gaussian and Markovian thus it fails to adequately describe systems with correlations, memory and spatial effects[9]. In fact, turbulent transport has been shown to be superdiffusive when it is close to marginal state and for weak mean/zonal flows; this effect was considered on the example of the gradient-induced instabilities[10–13] and dissipative trapped-electron modes (DTEM) instabilities[14–16]. On the contrary, turbulence induced transport across flows with sufficient shear tends to be subdiffusive; as it was demonstrated on some instances of the ion temperature-gradient modes (ITG)[17–21] or shear Alfvén, drift tearing and ballooning modes[22,23]. In the particular case of quasi-poloidally symmetric stellarator geometries, turbulent transport associated with supercritical ITG turbulence becomes subdiffusive[21] as the degree of quasi-poloidal symmetry increases triggering the effect of sheared flows. Also, a number of experimental and numerical studies at TORPEX[24–28] has demonstrated that suprathermal ion transport changes from being subdiffusive to superdiffusive depending on the ion energy and turbulent fluctuation amplitudes. Furthermore, while large intermittent and persistent $\mathbf{E} \times \mathbf{B}$ drifts lead to superdiffusion their suppression results in subdiffusion.

On the other hand, it was found[29] that the α-particle transport for realistic ITG and TEM turbulent regimes is diffusive and becomes significant only at energies ~ 100 keV. A recent work[30] shows clear indications of the non-diffusive nature of 3.5 MeV α-particle neoclassical transport; i.e. when transport originates from the averaged radial drifts due to the non-uniform three-dimensional magnetic field and not from the collisions dynamics, which is low enough to be neglected. This transport is of special relevance for stellarator geometries, whose non-axisymmetric character strongly impacts particle dynamics. In fact, the confinement of α-particles is one of the

most critical points in the design of a viable stellarator fusion reactor[7,31–34].

The aim of this work is to examine the collisionless α-particles neoclassical transport[30] by means of fractional transport theory adapting the techniques used in characterizing the non-diffusive dynamics of turbulent transport [9]. Of particular interest is the effect of the level of quasi-toroidal symmetry on the fractional transport coefficients. To this end, five configurations stepwise breaking the symmetry were considered: from a perfectly symmetric ITER tokamak model to four stellarator configurations with different levels of quasi-toroidal symmetry. Fractional transport coefficients were estimated applying Lagrangian and Eulerian techniques to a set of trapped α-particle trajectories corresponding to the largest fraction of losses obtained with the Monte Carlo orbit following code MOCA[30,35–37]. The set comprises only the confined part of these particle trajectories, i.e. before the particles are lost, to avoid contaminating the statistics with the effect of ripple at the outer radial positions, which leads to convective (ballistic) behavior.

The remainder of the paper is organized as follows. Section II presents the basic approximations used, the magnetic configurations considered and the numerical tools applied. The techniques of fractional transport theory and their application are described in Section III. A summary of the results is given in Section IV. The final Section V briefly discusses the validity of a non-diffusive approach in building an effective model of ripple-enhanced α-particle transport.

II. APPROXIMATIONS, MAGNETIC CONFIGURATIONS AND NUMERICAL METHODS

This section summarizes the main approximations used, introduces the magnetic configurations under study and the equations of motion of α-particles together with some details about the numerical neoclassical code MOCA.

The three approximations applied here are the *small gyroradius ordering*, neglecting the electric field and neglecting the α-particle collisions. Along with these approximations, throughout all simulations particles are considered monoenergetic and all perturbations (e.g. Alfvén, drift tearing, ballooning, ..., modes) are neglected. The spatial and temporal drift orderings are justified (except perhaps in the pedestal region) because of the ratio between, on the one hand, the large spatial scale lengths of field corrugations $L \sim 1$ m and orbit widths $L \sim 0.5$ m in reactor conditions with the α-particle Larmor radius $\rho_\alpha \sim 0.05$ m, and, on the other hand, the slow circulating $\tau \sim 5\mu$s, bouncing $\tau \sim 20\mu$s, collisional slowing-down $\tau_{slow} \sim 1$s and scattering $\tau_{scatt} \sim 5$s times compared

with the cyclotron times. The orbit widths, circulating and bouncing times were obtained in Ref.[30], while the slowing-down and scattering times correspond to typical reactor conditions, i.e. $n \sim 1$ and 5×10^{20} m^{-3} as $T \sim 25$ and 15 keV for tokamaks and stellarators respectively. The reason for ignoring electric field effects is the huge difference between the α-particle speed $v_\alpha \approx 1.3 \times 10^7$ m/s and the $\mathbf{E} \times \mathbf{B}$ drift speed, or either the unrealistic electric fields required to make them comparable. Finally, to focus only on the relation between the symmetry level of the magnetic configuration and α-particle dynamics, collisions will be neglected.

In this work, the magnetic configurations considered are based on an ideal ripple-less tokamak with ITER[38] parameters, $B \sim 5.3$ T, $a = 2.67$ m, $R = 6.2$ m and $V \sim 900$ m^3 (approximately corresponding to a $Q \approx 10$ and $I_p = 15$ MA scenario) and a quasi-toroidally symmetric (QTS) stellarator loosely based on a vacuum NCSX[39,40] project configuration and having the same nominal field and volume as ITER but a different size $a = 2.15$ m, $R = 9.8$ m. The structure of the magnetic field for these two configurations was obtained using the 3D ideal Variational Magnetohydrodynamic Equation solver Code VMEC[41] and thus excludes the existence of both islands and stochastic regions. Since the orbit following code MOCA works in Boozer coordinates, the two VMEC equilibria are decomposed in Boozer[42] magnetic flux coordinates using 1050 modes to guarantee a precise description of the equilibria. Notice, however, that the accurate calculation of particle trajectories, just depending on the magnetic field magnitude, requires much less modes than those needed to capture its three dimensional shape. Moreover, particle orbits depend on spatial scales larger than those needed for stability calculations (ballooning, peeling-ballooning, ...) where a precise representation of small scales is necessary to localize unfavorable regions on the flux surfaces.

Based on the neoclassical community experience[37], to accurately describe the *long mean free path* collisionality regime, similar in requirements to our analysis of collisionless α-particles, it is sufficient to consider only the Boozer normalized harmonics larger than a threshold $\delta = 10^{-3} - 10^{-4}$, even for stellarators as complex as TJ-II[35]. To be on the safe side, the smallest threshold $\delta = 10^{-4}$ was used to obtain the ITER and QTS72 magnetic field configurations which have seven and 72 modes respectively. Though this number of modes is insufficient to capture the smallest spatial scales of the original equilibrium, and cannot be used to perform any stability calculations, it is adequate to describe the original VMEC equilibrium magnetic field and provides the two references for our work: an ideal axisymmetric tokamak and a realistic quasi-toroidally symmetric stellarator. Nevertheless, to be sure that the configuration QTS72 was sufficiently close to

the original QTS equilibrium, all the procedures described in this work were applied to a magnetic field configuration obtained with $\delta = 10^{-5}$ and having 197 modes, giving results almost identical, within the error bars, to that of QTS72. Since both, the full QTS and QTS72 magnetic field configurations are relatively far from being axisymmetric, see Figure 1, the strategy followed to study the effect of approaching quasi-toroidal symmetry was to use the original Boozer decomposition of the QTS equilibrium and increase stepwise the threshold put on the normalized harmonics from $\delta = 10^{-4}$ of QTS72 to 1/180, 1/150 and 10^{-2} to obtain magnetic configurations with 6, 5 and 4 modes respectively, see Figure 1. This process guarantees that the ripples introduced by these modes are included based on their importance to the original QTS equilibrium. QTS4 contains the following four $B_{m,n}$ modes: $B_{0,0}$, $B_{1,0}$, $B_{2,0}$ and $B_{2,1}$, ordered in decreasing absolute value. QTS5 adds to those harmonics the mode $B_{1,-1}$ and QTS6 includes also $B_{3,2}$. The modes B_{mn} with $n \neq 0$ are the responsible of breaking the toroidal-symmetry. The five magnetic configurations considered in this work, namely ITER, QTS4, QTS5, QTS6 and QTS72 are the same used in Ref[30] and though none of them are exact solutions of the original QTS VMEC equilibrium, they share the same dominant modes (by construction), have the same basic field structure and results in magnetic configurations with increasing degree of quasi-toroidal symmetry σ_{qt}, shown in Figure 1 and defined as:

$$\sigma_{qt}(\psi) = \frac{\sum_{m=1}^{M} |B_{m0}(\psi)|}{\sum_{n=1}^{N} |B_{0n}(\psi)| + \sum_{m=1}^{M} \sum_{n=-N}^{N} |B_{mn}(\psi)|} \tag{1}$$

In the small gyroradius approximation, the motion of collisionless α-particles in the aforementioned magnetic configurations is described by the next two equations. One for the guiding center position $\mathbf{r}_g$

$$\dot{\mathbf{r}}_g = pv\frac{\mathbf{B}}{B} + \frac{mv^2}{2qB^3}(1+p^2)\mathbf{B} \times \nabla B \tag{2}$$

and another for the pitch $p = v_{\parallel}/v$ (it should not be confused with the usual definition for the canonical momentum P)

$$\dot{p} = -\frac{v}{2B^2}(1-p^2)\mathbf{B} \cdot \nabla B \tag{3}$$

where the dot implies derivative with respect to time, v and q are the speed and charge of the particle and $\mathbf{B}$ and B are the magnetic field and its magnitude. Notice that no equation is required for the evolution of the particle speed since electric field and collisional effects are neglected.
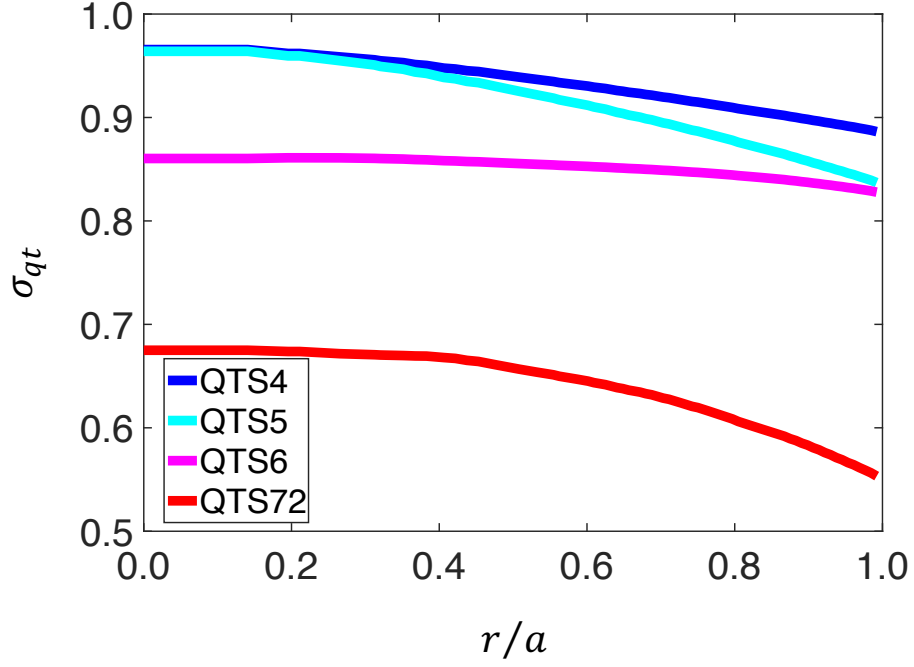
FIG. 1. Quasi-toroidal symmetry ratio σ_{qt} for the four quasi-toroidal stellarators as a function of radial coordinate r/a.

These two equations reduce to a set of four coupled ordinary differential equations depending on the field strength $B(\psi, \theta, \varphi)$ and it derivatives with respect to the radial ψ, poloidal θ and toroidal φ spatial Boozer coordinates. For every magnetic configuration, the transport was modeled by an ensemble of α-particles, whose trajectories are simulated integrating this system of ODEs with the Monte Carlo code MOCA. A parallel FORTRAN code working in Boozer coordinates that uses a three-dimensional grid $N_\psi \times N_\theta \times N_\varphi \equiv 100 \times 360 \times 360$ per machine period to pre-store and interpolate the magnetic field magnitude and its derivatives using the Bulirsh-Stoer algorithm[43] to integrate particle trajectories.

In all simulations presented, α-particles are initialized at the half-radius $r/a = 0.5$ with a fixed energy of 3.5 MeV. They are distributed uniformly in pitch and randomly in poloidal angle for ITER (65536 particles) and in poloidal and toroidal angles for the stellarator cases (262144 particles each). The random distribution used for the poloidal and toroidal angles has been chosen to be inversely proportional to the Jacobian, $1/J(\psi, \theta, \varphi) = (B(\psi, \theta, \varphi)/B_0)^2$, of the coordinate transformation to keep a uniform density on the flux surface in real space, thus initializing more particles in regions of higher magnetic field. The time step used, $\Delta t \approx 10^{-8}$ s, was the result of a

trade-off between the orbit following code integration accuracy (measured with the relative change in particle energy during their lifetimes, which was kept below $\sim 10^{-5}\%$) and the total simulation time, which was chosen to ensure that no new *regimes* appear in the cumulative loss fraction of particles for any configuration, see Figure 2. The actual value used, $t = 10$ s was the result of a rather long simulation performed for QTS4 (the one with the expected longer saturation time) and suffices to guarantee that the *plateau* was fully achieved for QTS72 and QTS6 and fairly indicated for QTS5 and QTS4. All results were checked to be independent of the number of particles considered and the grid size and grid interpolation scheme applied to define the 3D magnetic field.
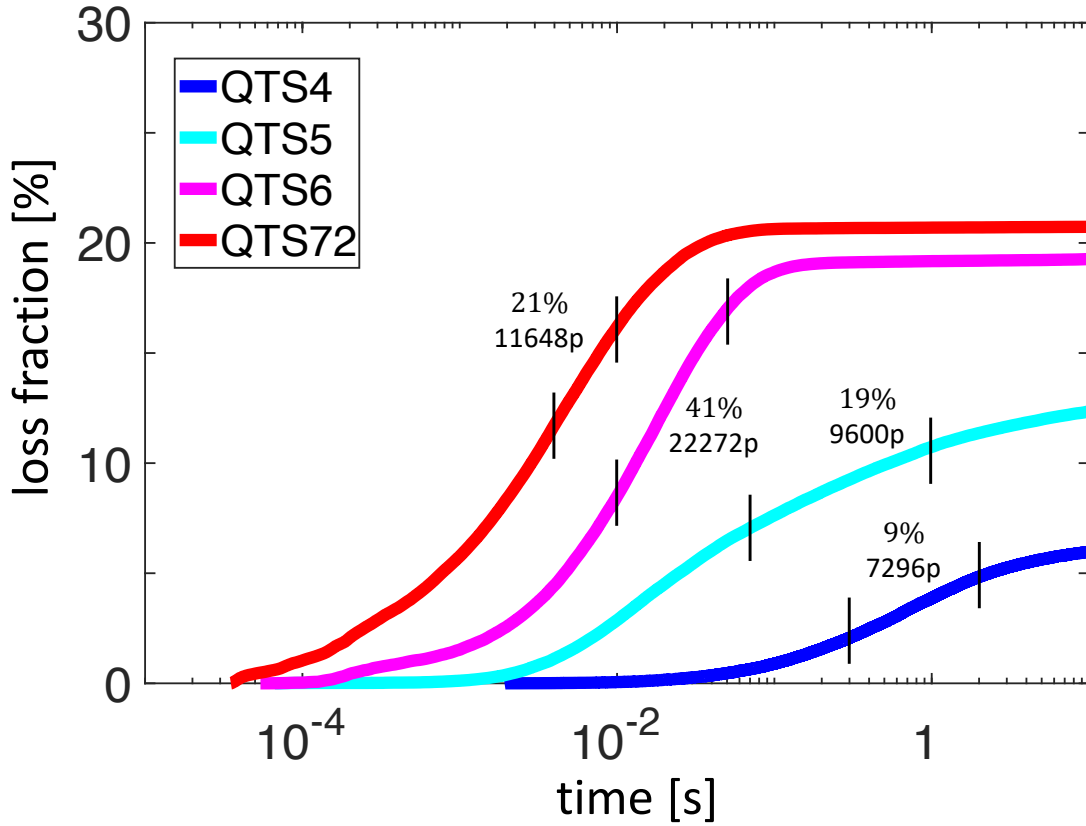

FIG. 2. Loss fraction of α-particles over time for the four quasi-toroidal stellarators. Vertical lines indicate the exit-time range of the particles considered for the fractional transport analysis, whose number and percentage among trapped particles are given for each configuration, the first (left) vertical lines correspond to the simulation time of the selected α-particles.

In all five configurations, particle trajectories can be broadly classified into two groups as those that keep or change their initial pitch sign, called *passing* and *trapped* respectively. Notice that the

latter naming convention differs from the one commonly associated with the parallel dynamics in neoclassical theory[44–46]. In the quarter million particles used for the simulations, these two types of trajectories can be further subdivided into finer kinds of executed orbits[1]: passing, stagnation, potato, ripple trapped, bananas, ... and combinations between them since particles can change their orbits from one type to another during their lifetimes, even without considering collisions. Before trying to characterize α-particle transport, it is necessary to classify the fractions of the different types of particle trajectories and followed orbits since their confinement varies. For example, the average radial drift of collisionless passing and stagnation orbits is negligible compared to that of banana or ripple trapped orbits, mixing them in a unique analysis could contaminate the statistics and mask the transport dynamics of interest.

Firstly, we have calculated the cumulative fraction of loss particles, see Figure 2. For ripple-less ITER not even a single particle is lost during the simulation, which is also an efficient test to demonstrate the fairly low numerical diffusion of MOCA. For the four QTS configurations, the trend shows that the decrease in symmetry level leads to larger losses. This can be explained by the fact that confinement relies on ensemble average radial drifts. For a toroidally symmetric configuration, like ripple-less ITER, the radial average automatically cancels, but as soon as symmetry is broken, as for the other four configurations considered, the radial average rapidly increases. The different slopes in Figure 2 indicate that the particle escaping rates vary, contributing in different ways to the transport.

Secondly, particle orbits are classified in two basic types: trapped and passing, depending on whether they change, or not, the sign of their pitch respectively. We found that not a single passing particle was lost for any configuration. While the fraction of trapped particles in ITER is $\sim 30\%$ and all are perfectly confined, in the QTS configurations it is $\sim 20\%$ and the lost fraction increases as the level of quasi-symmetry decreases. A study was done for the five configurations with a newly developed numerical procedure that classifies and characterizes particle orbits, based on the analysis of reflection points and the poloidal angle at which they cross (or not) the equatorial plane between consecutive reflection points. The analysis of all trapped particle trajectories in the five configurations shows that more than a 90% of their orbits are either bananas or ripple trapped. As an example, Figure 3 presents two trapped α-particle trajectories with adjacent initial conditions, where one escapes following solely banana orbits and the other eventually transitions its orbit to the ripple trapped. No further attempt was made to distinguish the other 10% of orbit types. More in detail, two limiting cases are found, on the one hand, ITER with 97% of bananas and zero ripple

trapped orbits, and, on the other hand, QTS72 with 54% bananas and 35% ripple trapped orbits. The procedure also allows to estimate the width and center of banana orbits, see Ref.[30] for details and other orbit examples.
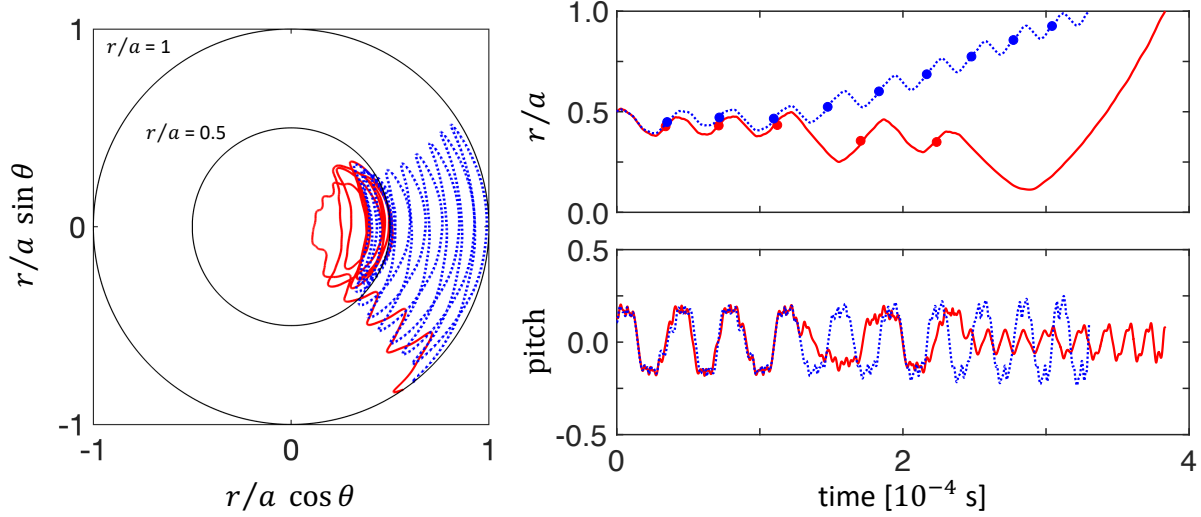

FIG. 3. Left: poloidal projection of two trapped α-particle trajectories with adjacent initial conditions in Boozer coordinates for the QTS72 configuration from their initialization at $r/a = 0.5$ till their lost at $r/a = 1$. Blue/dashed trajectory follows only banana orbits, red/solid trajectory follows banana orbits and shortly after 0.2 *ms* becomes ripple trapped. Right: time evolution of the radial position r/a (top) and pitch (bottom) of the same trajectories. The centers of all the banana orbits are indicated by the circles (top).

Lastly, with the aim to evaluate particle transport, it is necessary to select the kind of particles and time scales of interest for a given configuration. With this in mind, neither passing particles nor particles belonging to the saturation region in Figure 2 contribute to transport and, therefore, will be ignored together with the prompt losses, who's established *convective* behavior would only mask the results. To characterize the relevant transport parameters, the region with the steepest slope in the loss fraction is chosen; i.e. the range belonging to the largest fraction of particle losses. The analysis of Section III will be performed on the trajectories of all trapped particles which are lost in the interval marked with vertical black lines in Figure 2. The number of particles considered in each QTS configuration and their percentage among trapped particles are also indicated in the figure. Despite the fact that collisionless α-particles in ITER lack any kind of transport, a set consisting of $\sim 20,000$ trapped particles will be analyzed for testing purposes.

9

III. FRACTIONAL TRANSPORT DIAGNOSTICS

In this section we will provide a brief introduction to the basics of the fractional transport equation and to some methods to estimate its exponents by means of tracked particles. These are the methods that will be used in the reminder of the paper to analyze the characteristics of the transport of α-particles.

A. Fractional transport equation and transport exponents

A well-known example of the mathematical relation between some macroscopic transport equations and certain features of its microscopic transport dynamics is the classical diffusion equation,

$$\frac{\partial n}{\partial t} = D\frac{\partial^2 n}{\partial x^2} \tag{4}$$

where D is the classical diffusion coefficient. Although the validity of this equation could be assumed ad-hoc, it can also be easily derived from stochastic or probabilistic descriptions of the underlying microscopic transport process. For example, it can be obtained from the classical continuous-time random walk (CTRW)[47], that describes the motion of a population of walkers that execute jumps of length Δx after having waited at their current location for an amount of time Δt. The probability density distributions (pdfs) of steps, $p(\Delta x)$ and waiting times, $\psi(\Delta t)$ define the CTRW. Not every CTRW results in a macroscopic diffusion equation. But in the case of a symmetric CTRW (i.e., the jump pdf has zero mean), if both jumps and waiting-times are uncorrelated and have a well-defined associated scale, given by the (square-root of the) variance of step pdf, σ, and the mean of the waiting-time pdf τ. It is readily found that the motion of the microscopic walkers is well-described by Eq. 4 for long times and distances. In fact, $D \propto \sigma/\tau$. Mathematically speaking, these conditions translate into the need for the step-size pdf of being within the basin of attraction of the Gaussian distribution of the same variance, as dictated by the central limit theorem, and the waiting-time pdf to be in the basin of the exponential pdf with the same mean[48].

If the macroscopic transport exhibits features such as the presence of long temporal correlations or an apparent lack of characteristic scales, it should then be expected that Eq. 4 provides a poor description of the transport dynamics. It has been suggested by many authors that, in these cases,

a more general transport equation is needed. One possibility is the fractional transport equation,

$$\frac{\partial n}{\partial t} = D_t^{1-\beta}\left[K\frac{\partial^\alpha n}{\partial |x|^\alpha}\right], \quad 0 < \beta < 1, \, 0 < \alpha < 2, \tag{5}$$

where D_t^γ represents the fractional Riemann-Liouville operator of the order γ, K is a constant and $\partial^\alpha n/\partial |x|^\alpha$ is the Riesz fractional derivative of the order α [49]. Fractional operators are integro-differential equations so that the temporal fractional derivative integrates over the full history of the system, thus being able of including memory effects. Similarly, spatial fractional derivatives integrate over the whole system domain and can capture non-local effects.

The convenience of using fractional transport equations can be justified similarly to how we previously did for the classical diffusion equation. Starting with the usual CTRW, Eq. 5 can be obtained as its long-time, long-distance limit whenever one introduces the observed lack of characteristic scales by choosing step-size pdfs with diverging variance, (i.e., $p(\Delta x) \sim \Delta x^{-(1+\alpha)}$, $0 < \alpha < 2$) and waiting-time pdfs with divergent means (i.e., $\psi(\Delta t) \sim \Delta t^{-(1+\beta)}$, $0 < \beta < 1$) [50]. Mathematically, this is again tantamount to choosing them from within the basin of attraction of the proper subfamily of Lévy pdfs[48] as dictated by the generalized central limit theorem.

The exponents α and β in Eq. 5 are known as fractional transport exponents. In the limit $\alpha \to 2$ and $\beta \to 1$, the usual classical diffusion equation is recovered. However, if $\alpha < 2$, non-local spatial effects are relevant. Similarly, if $\beta < 1$, memory effects are essential in determining future transport. It is also common to define a third exponent, $H \equiv \beta/\alpha$, known as the Hurst exponent[51]. For the diffusive case, $H = 1/2$. Therefore, any equation with $H > 1/2$ is usually referred to as superdiffusive, and subdiffusive if $H < 1/2$. These transport dynamics has very interesting features. For instance, perturbations can spread in them very quickly (superdiffusion) or extremely slowly (subdiffusion). In the former case, they can resemble avalanche-like transport while in the latter, they may exhibit extreme stickiness. For that reason, they are used to model transport in situations in which these features are known to exist[50,52].

The best manner to test whether Eq. 5 provides a good model for transport in any system is to estimate the values of the fractional transport exponents that best reproduced its observed transport features. There are a few methods to do this, most of them based on specific features of Eq. 5 and its propagator, $P(x,t)$. The propagator of any differential equation is the temporal evolution of its initial conditions. Or, in other words, the probability of finding at time t a particle at position x if it was initially at x_0. Values of the fractional exponents that best model transport in any system can then be obtained with relative ease by comparing the propagator of Eq. 5 with some numerical

reconstruction of the propagator in the system of interest, usually by employing tracked or tracer particles. A review of many of these techniques can be found elsewhere [9], but we will focus on two of them in what follows.
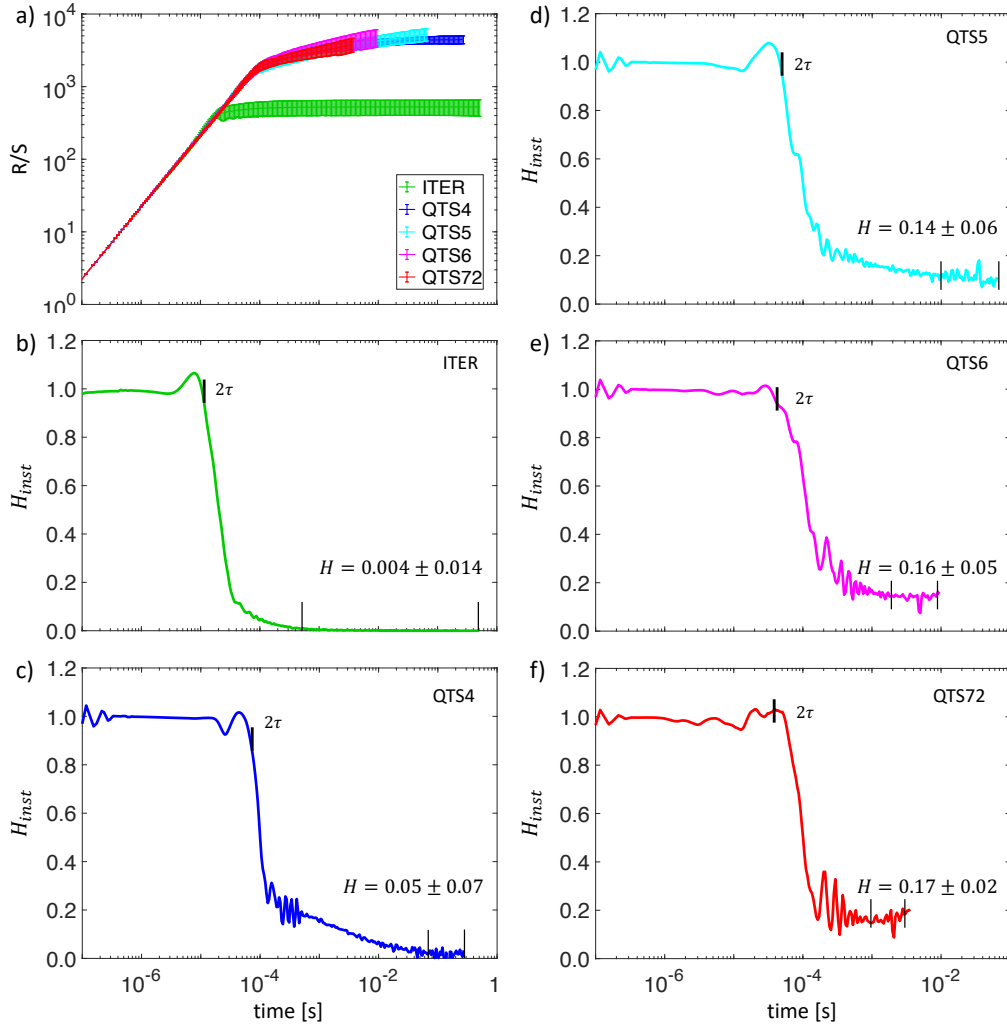
B. The Eulerian method

FIG. 4. Rescale range analysis (a) and instantaneous Hurst exponent, $[R/S] \sim \tau^H$, for ITER (b), QTS4 (c), QTS5 (d), QTS6 (e) and QTS72 (f), τ_b is the characteristic bouncing time. Vertical lines indicate fitting range, i.e. the mesoscale, for the resulting Hurst exponent H.

The Eulerian method relies on exploiting some scaling properties of the propagator of Eq. 5. In

particular, it can be shown that, for fixed time t_i the propagator scales as[11,53]:

$$P(x,t_i) \sim |x-x_0|^{-(1+\alpha)}, \quad |x-x_0| \gg K^{1/\beta} t_i^{\beta/\alpha} \tag{6}$$

from where α could be found by fitting the tail of the propagator $P(x,t_i)$ to a power law in log-log scale. The derivative of the propagator at fixed time gives the local spatial exponent:

$$\alpha(x) = -\left[1 + \frac{x}{P(x)} \frac{dP}{dx}\right] \tag{7}$$

that should come out to be rather independent of x (or at least over a sufficiently long range) to be meaningful.

To apply this method to our system of interest, one could follow a population of N tracked particles in time, record their trajectories $x_j(t)$, $j = 1, \cdots, N$, and then build an approximation of the propagator simply by building the probability density function of $x_j(t) - x_j(0)$. The tail of the resulting pdf, at sufficiently long times, should behave as Eq. 6 if the fractional transport equation does provide a reasonable model for transport in the system.

The temporal exponent, β, can be estimated in a similar way using another scaling property of the propagator of Eq. 5. For any fixed location, x_i, that is sufficiently far from x_0 the propagator scales as[11,53]

$$P(x_i,t) \sim t^{\beta}, \quad t \ll K^{1/\beta} x_i^{\alpha/\beta}, \tag{8}$$

and,

$$P(x_i,t) \sim t^{-\beta}, \quad t \gg K^{1/\beta} x_i^{\alpha/\beta}. \tag{9}$$

Thus, one could in principle estimate β by following in time the value of the numerical propagator, constructed as we discussed earlier, at any fixed location.

The Hurst exponent can be estimated as the ratio $H = \beta/\alpha$ once their values are available from the determinations previously described. But it can also be estimated directly from the numerical propagator. Indeed, yet another property of Eq. 5 is that all finite moments of its propagator satisfy,

$$\int |x-x_0|^{\mu} P(x,t_i) dx \propto t^{\mu H}, \quad 0 < \mu < \alpha. \tag{10}$$

Since the determination of β is usually the most challenging one from a practical point of view, it is sometimes preferable to determine H using Eq. 10, and then infer it via the relation $\beta = \alpha H$.
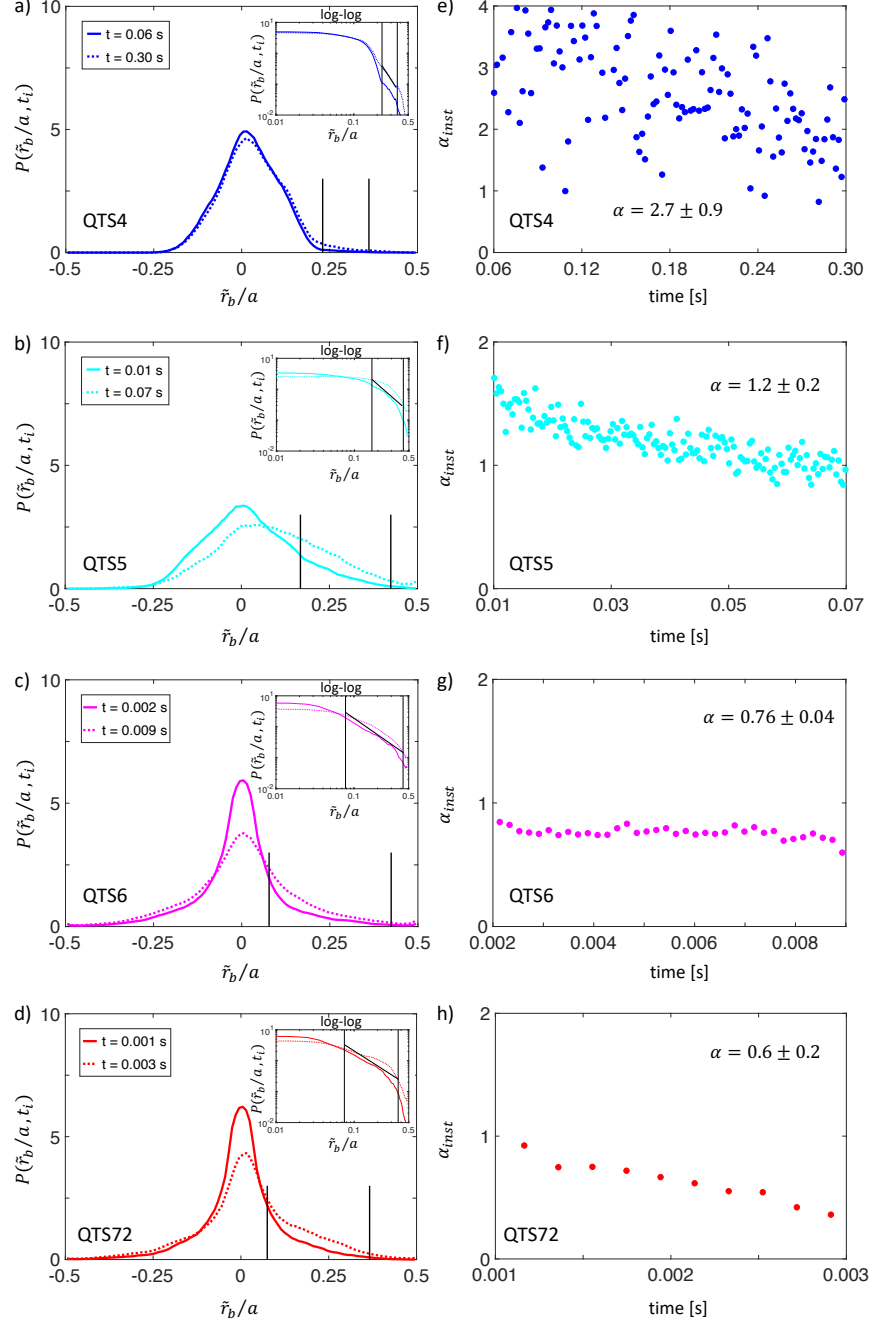
FIG. 5. Left: Propagator constructed as density function of normalized banana centers $\tilde{r}_b/a$ at the beginning and end of the *mesoscales* for QTS4 (a), QTS5 (b), QTS6 (c) and QTS72 (d) in linear and logarithmic scales. Vertical lines indicate fitting range for the exponent α. Right: Instantaneous spatial exponent and its averaged over the mesoscale value α for QTS4 (e), QTS5 (f), QTS6 (g) and QTS72 (h).

14

C. The Lagrangian method: R/S analysis

There is another way to estimate H that does not require the calculation of the numerical prop-
agator, but that can be directly inferred from the analysis of the trajectories of individual tracked
particles or, more precisely, their instantaneous velocities[15]. In particular, H can be obtained by
performing the so-called rescaled range analysis[51] on the velocity of each particle, and then aver-
aging over as many particles as are available. The procedure for a single particle is to consider the
velocity series $\{V_k = x_{k+1} - x_k, k = 1, 2, \ldots, N\}$ of each tracked particle, and calculate its rescaled
range at iteration $k = \tau$ using:

$$[R/S](\tau) = \frac{\max\limits_{1 \leq k \leq \tau} W(k, \tau) - \min\limits_{1 \leq k \leq \tau} W(k, \tau)}{(\langle V^s \rangle_\tau - \langle V \rangle_\tau^s)^{1/s}} \tag{11}$$

where,

$$W(k, \tau) = \sum_{i=1}^{k} V_i - k \langle V \rangle_\tau \tag{12}$$

and $\langle \cdot \rangle_\tau$ represents the average up to iteration τ. The denominator is the fractional standard devia-
tion of order $0 < s < \alpha$[16]. If transport is indeed scale-free and governed by an equation similar to
Eq. 5, one should find that $[R/S] \sim \tau^H$ (with $H = \beta/\alpha$) over a meaningful range of times[15], from
which the fractional exponent H can be inferred. It is also possible to determine the instantaneous
Hurst exponent via:

$$H(\tau) = \frac{\tau}{[R/S](\tau)} \cdot \frac{d[R/S]}{d\tau}(\tau), \tag{13}$$

that should be rather independent of τ, at least over a sufficiently large range, to be meaningful.

D. On the sensitivity and validity of methods

To what extent can one trust the results of the previous analysis to estimate transport exponents?
First of all, any scaling exponent will only be meaningful if it remains valid over a sufficiently
large range of the relevant scale, usually referred to as *mesoscale*. It is difficult to define what
"sufficiently large" is in most cases, but we would require at least half, if not a full decade.

Secondly, the methods previously described can be proved to yield the same results only for
Eq. 5, that exhibits scale-invariance for all scales. This is not the case in any real system, that will
exhibit scale-invariance at best for a finite range of scales. In that situation, the values obtained
with the different methods may vary. In fact, the Eulerian and Lagrangian methods have different

sensitivities. Any method based on propagators usually is quite sensitive to finite-size effects, particularly if the system size is not too large. Rescaled-range analysis is usually much more robust, being rather insensitive to the presence of boundaries as well as other noise sources but feels the presence of any periodic contamination rather strongly. It also tends to work best at values of $H \sim 0.5$, but somewhat overestimates the exponent for $H < 0.3$ and underestimates it for $H > 0.8$[9]. It is important to be aware of these limitations when interpreting the obtained values of transport exponents while using the aforementioned methods.
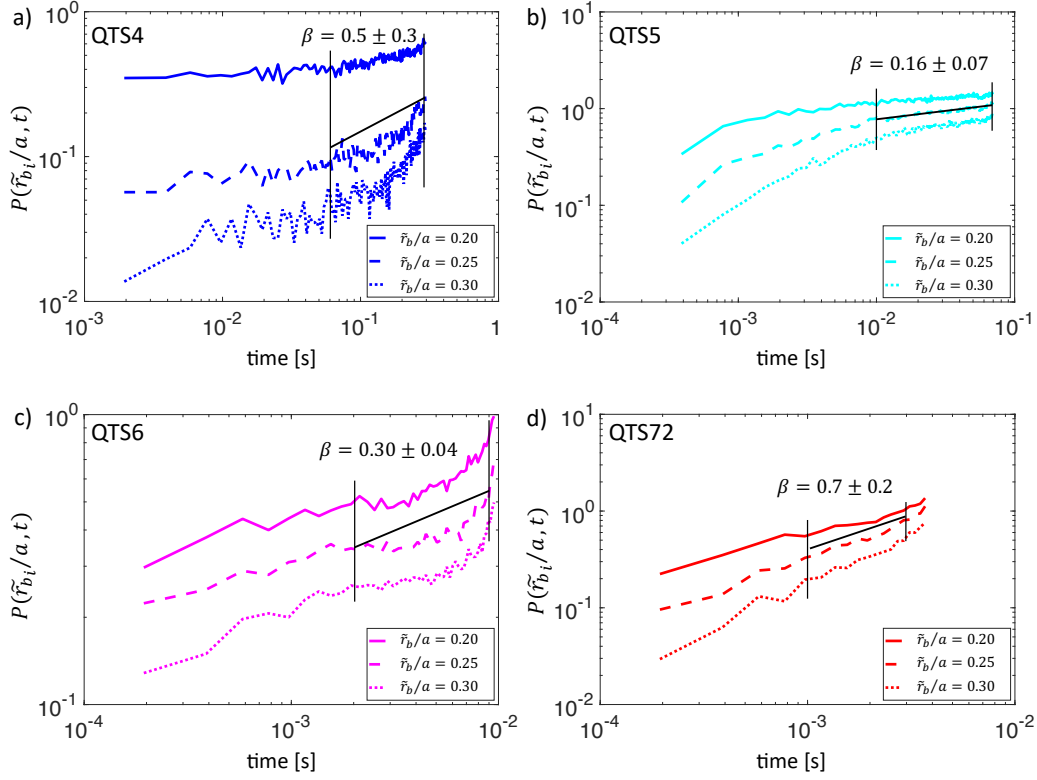

FIG. 6. Propagator of the banana centers for three fixed radial positions and averaged temporal exponent β fitted over mesoscale for QTS4 (a), QTS5 (b), QTS6 (c) and QTS72 (d).

IV. RESULTS

We analyzed a set of trapped α-particles for QTS configurations, whose exit-times are marked by the vertical lines in Figure 2, where the first (left) vertical lines correspond to the simulation time of the selected α-particles being 0.004 s, 0.01 s, 0.07 s and 0.3 s for QTS72, QTS6, QTS5 and QTS4, respectively, before losses occurs to avoid any biasing (particularly to avoid contaminating

16

the statistics by ripple trapped orbits, which have convective behaviour at the end of particle life-times). For ITER we characterized all trapped particles $\sim 20,000$ for half a second since they are perfectly confined. The Lagrangian Rescale range $[R/S]$ diagnostic described in Section III was performed using $r_g^{k+1} - r_g^k$ as V_k in Equation 11, which is proportional to the radial guiding center speed $\dot{r}_g$. On the other hand, the Eulerian technique was performed by constructing the propagator of the banana centers , $P(\tilde{r}_b/a, t)$, as $x - x_0 = \tilde{r}_b/a$. Here $P(\tilde{r}_b/a, t)$ is the probability density function of the normalized radial displacements of the banana orbit centers with respect to their initial positions at time t. This is done because the dynamics of the guiding center radial transport and the banana-centre motion are different for times shorter than the average banana orbit time, but become identical at longer times scales. The reason is that a banana-centre barely moves during the banana orbiting, while the guiding centre is moving back and forth in radius, as it follows the banana. The relevant transport dynamics happen in the mesoscale range, which is well be-yond the banana orbit time. In the calculation of the Hurst exponent, the coexistence of these two process at different timescales does not really alter the procedure, since they appear separated at different scaling ranges. For the calculation of the propagator, however, the two processes become more mixed, since the propagator calculated with guiding centres will be significantly deformed at the earlier timescales due to the back and forth motion, making more complicated the analysis at longer timescales. This distortion can be easily removed by considering only the banana center motion. Moreover, the displacement is computed with respect to its initial position instead from the position at the beginning of the mesoscale range since the calculation is approximately invari-ant under time-translations and it is difficult to specify the start of the mesoscale. The Eulerian method was applied solely for the QTS configurations due to the lack of any radial propagation of these orbits and the absence of stochastic tip diffusion[6] in perfectly axisymmetric ITER. The resulting transport exponents were estimated over the mesoscale range (indicated in all following figures).

A. The Lagrangian method: R/S analysis

The $[R/S]$ functions for the five configurations under consideration (all calculated with a fixed parameter $s = 0.3$ in Eq. 11 for consistency with the Eulerian method as $0 < s < \alpha$) are shown in the top left plot of Figure 4. The fact that the $[R/S]$ function changes its slope in ITER five times faster compared to the results for the four stellarators is pointing out to their quite different

17

transport time scales. This can be more clearly seen in the instantaneous Hurst exponents obtained according to Eq. 13 and also shown in Figure 4. The sharp drop from the ballistic phase with $H = 1$ should be related to the underlying banana orbits. Indeed, the steep plunge in H occurring at ~ 10 μs for ITER and between 40 and 60 μs for the stellarators corresponds to the time necessary to complete one full banana orbit, $2\tau_b$ (i.e. two bouncing times), estimated according to the connection lengths of the magnetic field lines Ref.[30]. Moreover, the difference between these values and the oscillations seen after the decay around $\gtrsim 100$ μs can be attributed to helically trapped orbits with longer connection lengths and slower bouncing times.

The Hurst exponent was estimated as the average of the instantaneous H over the region where it stabilizes, i.e. the mesoscale, bounded by the vertical lines in Figure 4. The result for ITER, where $H \sim 0$, suggests pure intermittency, being a typical characteristic of harmonic functions and confirming that the *frozen* bananas in ITER lack radial displacements. The modest values of H for the stellarators point to subdiffusion with the clear trend of increasing Hurst exponent for decreasing level of toroidal symmetry, but always staying way below the diffusive threshold of $H = 0.5$.

B. The Eulerian method

In the absence of the radial propagation of trapped particles in ITER, the Eulerian method was applied only to the four QTS stellarators. To estimate all three fractional exponents for each configuration, we choose the same fitting range, i.e. the mesoscale, as the one used in the $[R/S]$ calculations of the previous subsection, see Figure 4. The fractional spatial exponent α was obtained by fitting the tail of the propagator at fixed times $P(\tilde{r}_b/a, t_i)$ to a power law according to Eq. 6. The propagator at the beginning and the end of the mesoscale is presented in the left plots of Figure 5 both in linear and logarithmic scales (in log-log scale the resulting power law fit is given by a tilted black line in between the vertical bars). The slight radial asymmetry of the spatial propagators is due to the inhomogeneity of the magnetic field, that makes radial displacements towards the inside and the outside not completely symmetric. The results show an increasing variation of $P(\tilde{r}_b/a, t_i)$ with decreasing level of quasi-toroidal symmetry. The instantaneous spatial transport exponents $\alpha_{inst}(t)$ are presented in the right plots of Figure 5 and obtained by fitting to a power law the propagator, $P(\tilde{r}_b/a, t_i) \sim \tilde{r}_b/a^{-(1+\alpha)}$, from the beginning until the end of the mesoscale in the spatial regions marked by vertical lines on the left plots. The very small difference in $P(\tilde{r}_b/a, t_i)$ for QTS4

during such long period corresponds to the the very narrow saturation range in the $[R/S]$, see Figure 4 (c), and translates in a large dispersion of $\alpha_{inst}(t)$ for this configuration. The large variation of α_{inst} for QTS72, varying from around 0.9 to 0.3, makes the results rather unreliable. Besides these difficulties, there is a clear trend in reducing α from around 2.7 to 0.6 as the quasi-toroidal symmetry decreases.

The Eulerian technique can also be used to obtain the fractional transport exponent associated with the temporal dependence, β, by fitting the time decay of the propagator $P(\tilde{r}_{b_i}/a,t)$ according to Eq. 8. We choose three radial positions, $\tilde{r}_{b_i}/a = 0.20$, 0.25 and 0.30, corresponding to the center of the regions used in estimating α enclosed by vertical lines on the left plots in Figure 5. The temporal exponent β was calculated by averaging the three values obtained from fitting $P(\tilde{r}_{b_i}/a,t) \sim t^\beta$ over the mesoscale, likewise, being delimited with vertical bars in Figure 6 together with the resulting power law fit given by a tilted black line in between the bars. The values estimated for QTS5 and QTS6 are $\beta \sim 0.2$, while the results for QTS4 and QTS72 are significantly larger $\beta \sim 0.5 - 0.7$, however, the standard deviations for them are larger as well.
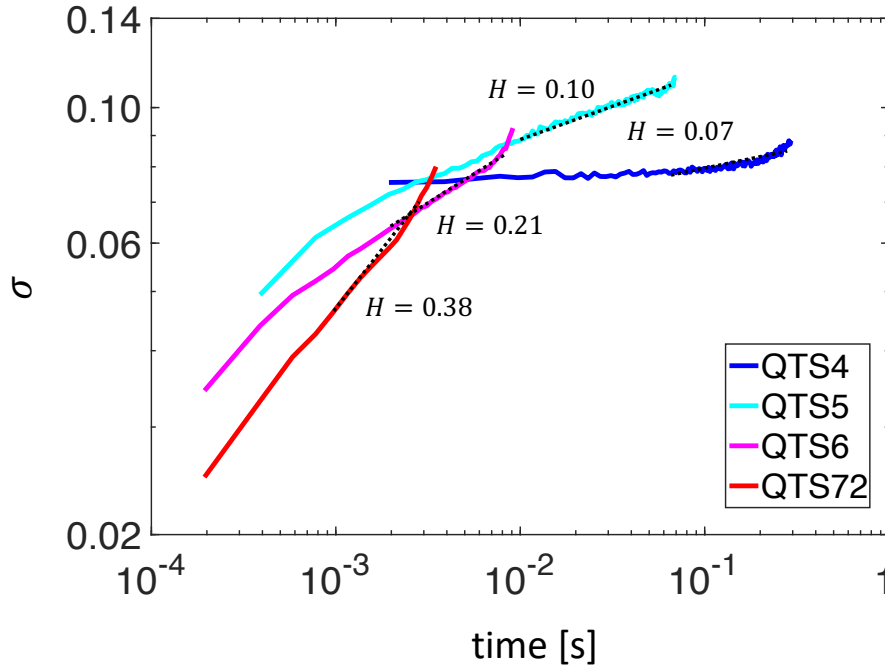

FIG. 7. Fractional standard deviation σ and the fitted over the mesoscale (indicated by dashed lines) Hurst exponent for the four stellarators.

Finally, it is possible to estimate the Hurst exponent from the time dependence of the fractional

standard deviation σ using Equation 10, i.e. the finite moment of the propagator of order less than α, according to the results depicted in Figure 6. The resulting fractional standard deviation is presented in Figure 7 in log-log scale along with the power law fit of H over the mesoscale and is calculated with $\mu_{QTS4} = 1.5$, $\mu_{QTS5} = \mu_{QTS6} = 0.5$ and $\mu_{QTS72} = 0.2$ each satisfying $\mu < \alpha$. As it was found previously by an alternative $[R/S]$ method, Hurst exponents increase as the stellarator configuration departs from quasi-toroidal symmetry but without exceeding the diffusive limit in $H = 0.5$ even for QTS72.

As a final part of our study, we also performed a rescaling of the propagator using the obtained fractional coefficients to confirm its good self-similar properties. A function $f(x)$ is called self-similar if $f(\lambda x) = \lambda^{-\gamma} f(x)$, where γ is called self-similarity exponent. In seeking for the self-similarity signatures of the propagator, we constructed the renormalized distribution $t^{\gamma} P(\tilde{r}_b/a, t)$, where as gamma we used either $\gamma = \beta/\alpha$ or $\gamma = H$ and plotted it as a function of the scaling variable $(\tilde{r}_b/a)/t^{\gamma}$ for the two time instances corresponding to the beginning and end of the mesoscale, see Figure 8 in a log-linear scale. In both cases, the distributions are far from having a Gaussian shape. However, the pdfs begin to resemble the parabolic profile with an increasing level of quasi-symmetry, which is also reflected by the increase of the estimated spatial exponent α that gradually approaches the value of two. In the limiting case of low symmetry for QTS72, the results with $\gamma = \beta/\alpha > 1$ are not reliable, while the results with $\gamma = H$ seem to be more trustworthy.

V. DISCUSSION AND CONCLUSIONS

The trajectories of collisionless trapped α-particles dictated by neoclassical theory for five magnetic configurations with different levels of toroidal symmetry have been analyzed with fractional transport tools to determine the effective nature of radial transport. The $[R/S]$ analysis applied to the perfectly confined trapped particles of the purely axisymmetric ITER tokamak results in a Hurst exponent $H = 0.004 \pm 0.014$ indicating ideal intermittency and the absence of radial transport. For this case, the Eulerian analysis becomes not feasible. The resulting Hurst exponents for the quasi-toroidal stellarators estimated by both the Lagrangian and the Eulerian techniques agree within the error bars except for QTS72, see Table I. This is possibly a consequence of its fast losses and the importance of finite size effects since propagator based estimations are quite sensitive to them, particularly if the system size is not too large. The values clearly suggest a subdiffusive transport behavior that becomes more pronounced as the level of quasi-toroidal symmetry
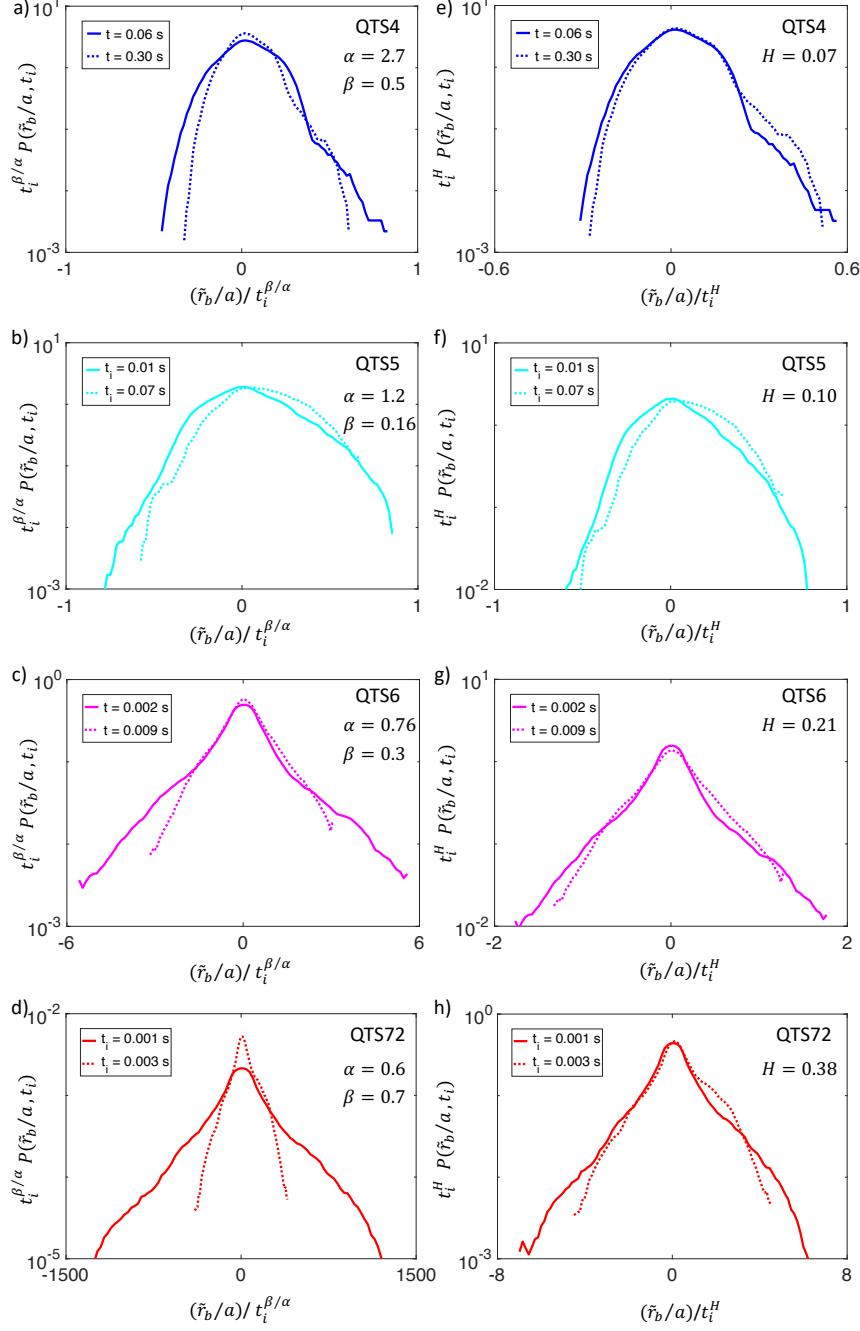
FIG. 8. Left: The renormalized distribution as a function of the similarity variable with $\gamma = \beta/\alpha$ for QTS4 (a), QTS5 (b), QTS6 (c) and QTS72 (d) in a log-linear scale. Right: The renormalized distribution as a function of the similarity variable with $\gamma = H$ for QTS4 (e), QTS5 (f), QTS6 (g) and QTS72 (h) in a log-linear scale.

increases.

The values of the spatial exponent α strongly decrease with decreasing symmetry and point to

	Lagrangian	Eulerian			
	H	H	α	β	$\beta = H * \alpha$
ITER	0.004 ± 0.014				
QTS4	0.05 ± 0.07	0.07	2.7 ± 0.9	0.5 ± 0.3	0.18 ± 0.06
QTS5	0.14 ± 0.06	0.10	1.2 ± 0.2	0.16 ± 0.07	0.12 ± 0.02
QTS6	0.16 ± 0.05	0.21	0.76 ± 0.04	0.30 ± 0.04	0.16 ± 0.01
QTS72	0.17 ± 0.02	0.38	0.6 ± 0.2	0.7 ± 0.2	0.24 ± 0.06

TABLE I. Transport exponents obtained by the Lagrangian and Eulerian techniques for the five configurations.

the presence of spatial correlations and the non-local nature of transport for these configurations. One might infer that the spatial exponent $\alpha = 2.7 \pm 0.9$ for QTS4 implies Gaussian statistics, but it is rather an artifact due to small broadening caused by the reduced average drifts for its highly quasi-toroidal symmetry. Additionally, in all cases the value of H stays well below $1/\alpha$, thus revealing the presence of strong anti-correlations[48].

The temporal exponent β deduced from the propagator analysis, see Table I, shows a large disparity between QTS5/QTS6 configurations where $\beta \sim 0.2 - 0.3$, and the limiting cases of high/low symmetry in QTS4/QTS72 with $\beta \sim 0.5 - 0.7$. As it was mentioned at the end of Section III B, the more reliable technique to obtain β is by using H and α values via $\beta = H\alpha$. As shown in the last column of the Table I, this technique offers values of $\beta \sim 0.2$ for the four QTS configurations. A reason for the large disparity between the QTS configurations estimated by the first technique (the propagator) could be related to the radial particle drifts. In particular, the β estimation may not be suitable for relatively slow particle drifts in QTS4 and, conversely, for fairly fast particle drifts in QTS72. On the other hand, both techniques are in good agreement for the QTS5 and QTS6 stellarators. In any case, the values of β for all configurations stay below 1 indicating a significant non-Markovian transport.

The difficulties encountered for QTS72 are a consequence of the fast losses due to its broken symmetry, which leads to short trajectories and a short range for the power law fits of $P(\tilde{r}_b/a, t)$ that can not capture the dynamics of α-particles in configuration accurately. On the other extreme is QTS4, whose high toroidal symmetry results in a minute variation of $P(\tilde{r}_b/a, t)$ leading to a large dispersion in the transport exponents. In between for QTS5 and QTS6, the resulting values

of the transport coefficients appear to be quite robust and consistent, considering both the Hurst exponents obtained by the Lagrangian and Eulerian methods and the β values estimated by the two techniques.

The results of our collisionless α-particle simulations, within the approximations used and the quasi-toroidally symmetric configurations examined, suggest that an increasing departure from quasi-toroidal symmetry results in faster and larger neoclassical losses. The analysis with fractional transport theory tools indicates that the transport of trapped but not prompt lost particles is non-Gaussian, non-Markovian and strongly subdiffusive. Moreover, fractional transport coefficients describe transport as becoming more subdiffusive as the level of the quasi-toroidal symmetry increases, which is similar to the results of Ref.[21] for supercritical turbulent transport in the presence of quasi-poloidal symmetry. Although, the validity of the fractional model itself becomes doubtful in the limiting cases of high and low symmetry.

ACKNOWLEDGMENTS

DATA AVAILABILITY STATEMENT

The data that support the findings of this study are available from the corresponding author upon reasonable request.

REFERENCES

[1]W. Heidbrink and G. J. Sadler, Nuc. Fusion **34**, 535 (1994).

[2]J. Jacquinot, S. Putvinski, G. Bosia, A. Fukuyama, R. Hemsworth, S. Konovalov, Y. Nagashima, W. M. Nevins, F. Perkins, K. Rasumova, F. Romanelli, K. Tobita, K. Ushigusa, J. W. V. Dam, V. Vdovin, and S. Zweben, Nuc. Fusion **39**, 2471 (1999).

[3]A. Fasoli, C. Gormenzano, H. Berk, B. Breizman, S. Briguglio, D. Darrow, N. Gorelenkov, W. Heidbrink, A. Jaun, S. Konovalov, R. Nazikian, J.-M. Noterdaeme, S. Sharapov, K. Shinohara, D. Testa, K. Tobita, Y. Todo, G. Vlad, and F. Zonca, Nuc. Fusion **47**, S264 (2007).

[4]V. Yavorskij, L. G. Eriksson, V. Kiptily, K. Schoepf, and S. E. Sharapov, J. Fusion Energy **34**, 774 (2015).

[5]R. J. Goldston and H. H. Towner, Journal Plasma Physics **26**, 283 (1981).

[6]R. J. Goldston, R. B. White, and A. H. Boozer, Phys. Rev. Lett. **47**, 647 (1981).

[7]C. D. Beidler, Y. I. Kolesnichenko, V. S. Marchenko, I. N. Sidorenko, and H. Wobig, Phys. Plasmas **8**, 2731 (2001).

[8]R. B. White and H. E. Mynick, Phys. Fluids B **1**, 980 (1989).

[9]R. Sánchez and D. E. Newman, Plasma Phys. Control. Fusion **57**, 123002 (2015).

[10]B. A. Carreras, V. E. Lynch, and G. M. Zaslavsky, Phys. Plasmas **8**, 5096 (2001).

[11]D. Del-Castillo-Negrete, B. A. Carreras, and V. E. Lynch, Phys. Rev. Lett. **94**, 065003 (2005).

[12]D. Del-Castillo-Negrete, Nonlinear Proc. Geoph. **17**, 795 (2010).

[13]L. Garcia and B. A. Carreras, Phys. Plasmas **13**, 022310 (2006).

[14]J. A. Mier, L. García, and R. Sánchez, Phys. Plasmas **13**, 102308 (2006).

[15]J. A. Mier, R. Sánchez, L. García, B. A. Carreras, and D. E. Newman, Phys. Rev. Lett. **101**, 165001 (2008).

[16]J. A. Mier, R. Sánchez, L. García, D. E. Newman, and B. A. Carreras, Phys. Plasmas **15**, 112301 (2008).

[17]X. Garbet and R. E. Waltz, Phys. Plasmas **5**, 2836 (1998).

[18]R. Sánchez, D. E. Newman, J. N. Leboeuf, V. K. Decyk, and B. A. Carreras, Phys. Rev. Lett. **101**, 205002 (2008).

[19]R. Sánchez, D. E. Newman, J. N. Leboeuf, B. A. Carreras, and V. K. Decyk, Phys. Plasmas **16**, 055905 (2009).

[20]R. Sanchez, D. E. Newman, J. N. Leboeuf, and V. K. Decyk, Plasma Phys. Control. Fusion **53**, 074018 (2011).

[21]J. A. Alcuson, J. M. Reynolds-Barredo, A. Bustos, R. Sanchez, V. Tribaldos, P. Xanthopoulos, T. Goerler, and D. E. Newman, Phys. Plasmas **23**, 102308 (2016).

[22] G. Sánchez Burillo, B. P. Van Milligen, and A. Thyagaraja, Phys. Plasmas **16**, 042319 (2009).

[23] G. Spizzo, R. White, M. Maraschek, V. Igochine, and G. Granucci, Nuc. Fusion **59**, 016019 (2018).

[24] K. Gustafson, P. Ricci, I. Furno, and A. Fasoli, Phys. Rev. Lett. **108**, 035006 (2012).

[25] A. Bovet, I. Furno, A. Fasoli, K. Gustafson, and P. Ricci, Nuc. Fusion **52**, 094017 (2012).

[26] A. Bovet, I. Furno, A. Fasoli, K. Gustafson, and P. Ricci, Plasma Phys. Control. Fusion **55**, 124021 (2013).

[27] A. Bovet, M. Gamarino, I. Furno, P. Ricci, A. Fasoli, K. Gustafson, D. E. Newman, and R. Sánchez, Nuc. Fusion **54**, 104009 (2014).

[28] I. Furno, A. Bovet, A. Fasoli, C. Gauthey, K. Gustafson, P. Ricci, and B. P. Van Milligen, Plasma Phys. Control. Fusion **58**, 014023 (2015).

[29] A. Croitoru, D. Padale, M. Vlad, and F. Spineanu, Nuc. Fusion **57**, 036019 (2017).

[30] A. Gogoleva, V. Tribaldos, J. Reynolds-Barredo, and C. Beidler, Nuc. Fusion **60**, 056009 (2020).

[31] S. V. Konovalov, E. Lamzin, K. Tobita, and Y. Gribov, in *28th EPS Conference on Contr. Fusion and Plasma Phys., Funchal, 18-24 June, ECA Vol. 25A* (2001) p. 613.

[32] M. Drevlak, J. Geiger, P. Helander, and Y. Turkin, Nuc. Fusion **54**, 073002 (2014).

[33] S. A. Henneberg, M. Drevlak, C. Nührenberg, C. D. Beidler, Y. Turkin, J. Loizu, and P. Helander, Nuc. Fusion **59**, 026014 (2018).

[34] M. Cole, R. Hager, T. Moritaka, S. Lazerson, R. Kleiber, S. Ku, and C. S. Chang, Phys. Plasmas **26**, 032506 (2019).

[35] V. Tribaldos, Phys. Plasmas **8**, 1229 (2001).

[36] V. Tribaldos and J. Guasp, Plasma Phys. Control. Fusion **47**, 545 (2005).

[37] C. Beidler, K. Allmaier, M. I. S. Kasilov, W. Kernbichler, G. Leitold, H. Maaßberg, D. Mikkelsen, S. Murakami, M. Schmidt, D. Spong, V. Tribaldos, and A. Wakasa, Nuc. Fusion **51**, 076001 (2011).

[38] J. M. Reynolds-Barredo, V. Tribaldos, A. Loarte, A. R. Polevoi, M. Hosokawa, and R. Sánchez, Submitted for publication to Nuc. Fusion (2020).

[39] M. C. Zarnstorff, L. A. Berry, A. Brooks, E. Fredrickson, G.-Y. Fu, S. Hirshman, S. Hudson, L.-P. Ku, E. Lazarus, D. Mikkelsen, D. Monticello, G. H. Neilson, N. Pomphrey, A. Reiman, D. Spong, D. Strickler, A. Boozer, W. A. Cooper, R. Goldston, R. Hatcher, M. Isaev, C. Kessel, J. Lewandowski, J. F. Lyon, P. Merkel, H. Mynick, B. E. Nelson, C. Nuehrenberg, M. Redi, W. Reiersen, P. Rutherford, R. Sanchez, J. Schmidt, and R. B. White, Plasma Phys. Control.

Fusion **43**, A237 (2001).

[40] B. E. Nelson, L. A. Berry, A. B. Brooks, M. J. Cole, J. C. Chrzanowski, H. M. Fan, P. J. Fogarty, P. L. Goranson, P. J. Heitzenroeder, S. P. Hirshman, G. H. Jones, J. F. Lyon, G. H. Neilson, W. T. Reiersen, D. J. Strickler, and D. E. Williamson, Fusion Eng. Des. **60-68**, 205 (2003).

[41] S. P. Hirshman, W. I. van RIJ, and P. Merkel, Computer Physics Communications **43**, 143 (1986).

[42] A. H. Boozer and G. Kuo-Petravic, *Physics of Fluids*, Phys. Fluids **24**, 851 (1981).

[43] W. H. Press, S. A. Teukolsky, W. T. Vetterling, and B. P. Flannery, *Numerical Recipes - The Art of Scientific Computing*, 2nd ed. (Cambridge University Press, 1994).

[44] A. A. Galeev and R. Z. Sagdeev, Sov. Phys. JETP **26**, 233 (1968).

[45] M. N. Rosenbluth, R. D. Hazeltine, and F. L. Hinton, Phys. Fluids **15**, 116 (1972).

[46] S. P. Hirshman and D. J. Sigmar, Nuc. Fusion **21**, 1079 (1981).

[47] E. Montroll and G. Weiss, J. Math. Phys. **6**, 167 (1965).

[48] G. Samoradnitsky and M. Taqqu, *Stable Non-Gaussian Random Processes: Stochastic Models with Infinite Variance*, Stochastic modeling (Chapman & Hall, New York, 2017).

[49] I. Podlubny, *Fractional Differential Equations* (Academic Press, 1998).

[50] R. Metzler and J. Klafter, Phys. Rep. **339**, 1 (2000).

[51] H. E. Hurst, Transactions of the American Society of Civil Engineers **116**, 770 (1951).

[52] R. Sánchez and D. Newman, *A Primer on Complex Systems - With Applications to Astrophysical and Laboratory Plasmas* (Springer Netherlands, 2018).

[53] D. Del-Castillo-Negrete, B. A. Carreras, and V. E. Lynch, Phys. Plasmas **11**, 3854 (2004).